Electronic Supplementary Material (ESI) for Journal of Materials Chemistry A.

Supplementary Materials for

Long-range oxygen ordering linked to topotactic oxygen release in $Pr_2NiO_{4+\delta}$ fuel cell cathode material

Rajesh Dutta, Avishek Maity, Anna Marsicano, Monica Ceretti, Dmitry Chernyshov, Alexeï Bosak, Antoine Villesuzanne, Georg Roth, Giuditta Perversi, Werner Paulus[1]

Correspondence to: werner.paulus@umontpellier.fr

This PDF file includes:

Figs. S1 to S7
Table S1

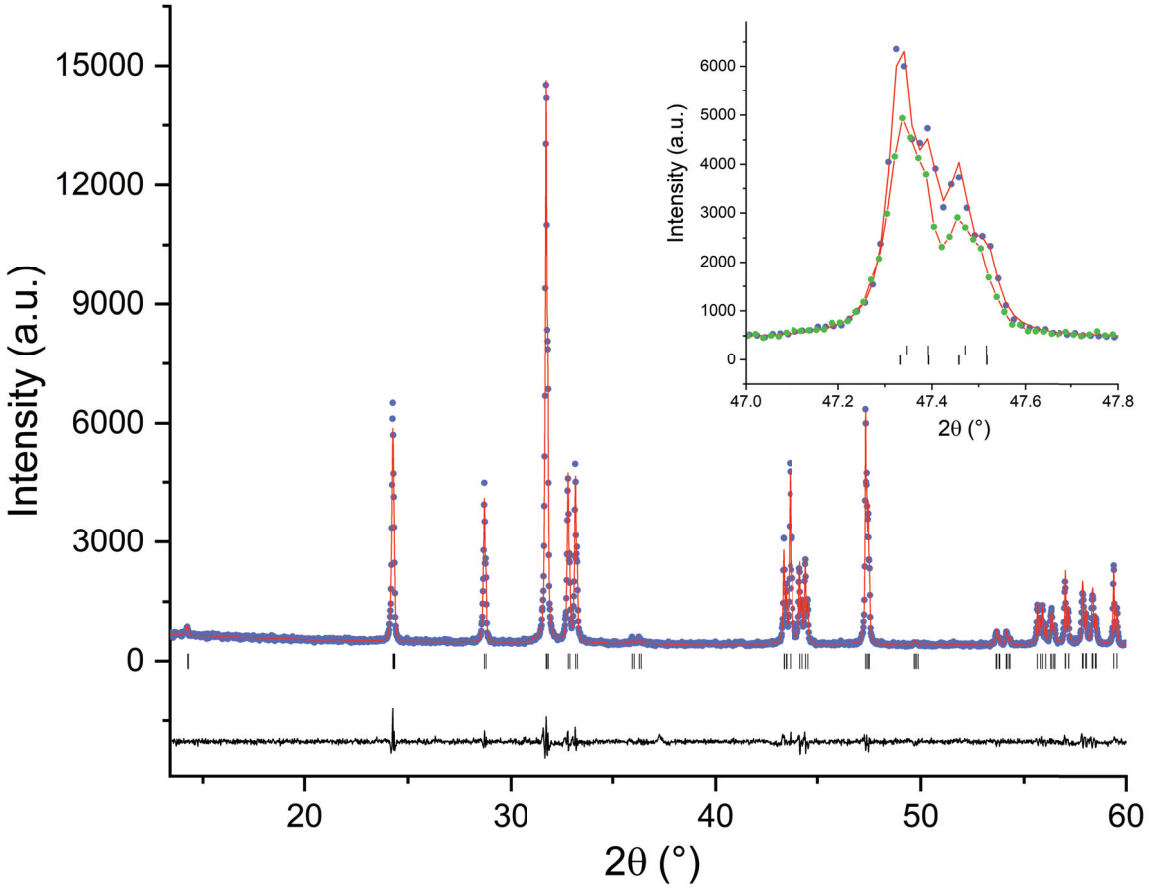

Fig. S1.

X-ray diffraction patterns of $Pr_2NiO_{4.225}$ (red line/light blue points) and $Pr_2NiO_{4.25}$ (inset only, all green), showing a monoclinic symmetry due to the splitting of the (220) reflections (see inset). XRD measurements were performed with a PANalytical X'Pert powder diffractometer (Cu $K_{\alpha 1,2}$).

The very similar lattice parameter for both phases were refined in the F112/m space group.

$Pr_2NiO_{4.225}$: a = 5.3945(4) Å, b = 5.4538(4) Å, c = 12.4408(10)Å, γ = 90.07(1)°),

$Pr_2NiO_{4.25}$: a = 5.3977(3) Å, b = 5.4540(3) Å, c = 12.4362(10) Å, γ = 90.03°(1)

Due to the small monoclinic deviation a proper assignment of the true symmetry becomes difficult with laboratory powder diffraction.

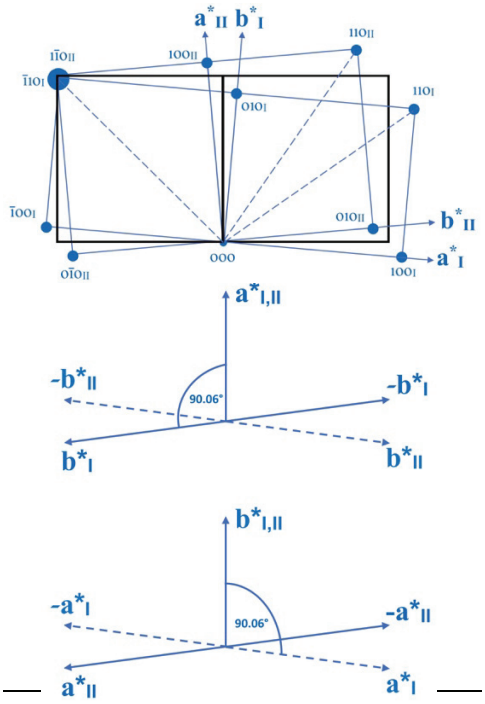

Fig S2: *(100)*- and *(010)*-twinning scheme for a monoclinic lattice, the small deviation from 90° is graphically exaggerated. In reality, an almost perfect overlap of (hkl) and $(h\bar{k}\bar{l})$ reflections is achieved in the upper case, while for the lower figure this is true for couples of (hkl) and $(\bar{h}k\bar{l})$ reflections, the c-axis being the monoclinic axis. The loss of the mirror plane in the *(a,c)*- or *(b,c)*-plane of the orthorhombic phase, is then at the origin of the creation of the common plane for the monoclinic twin individuals. The proximity of the monoclinic angle to 90° renders this type of twinning to be taken as merohedral. Since $(\bar{h}k\bar{l})$ and $(h\bar{k}\bar{l})$ in a setting with a monoclinic c-axis are not equivalent by symmetry, both twin configurations finally deliver for this type of merohedry a different structure factor for overlapping reflections. In addition, it is difficult to determine the volume fraction of the respective two twin individuals. Both arguments taken separated or together, result in the important consequence to not allow to separate related superimposed intensities of the superstructure reflections, since there is always an almost perfect superposition of pairs of non-equivalent (hkl) and $(\bar{h}k\bar{l})$ in case of *(010)*-twinning as well as (hkl) and $(h\bar{k}\bar{l})$ reflections for *(100)*-twinning, rendering difficult further structure analysis beyond an average structure model. The given twinning scheme yields for each orthorhombic twin domain a maximum of 4 monoclinic twin domains, which could then result, in the presence of 4 orthorhombic twin domains, to a total number of 16 monoclinic domains. In case of a non-centrosymmetric space group this number would get even increased to 32. A macroscopic consequence of the twinning is the “appearance” of a second orientation of each incommensurate diffraction vector, resulting from the common *(a,c)* and/or *(b,c)* twin-planes and which corresponds in its orientation as being “mirrored” at these respective planes.

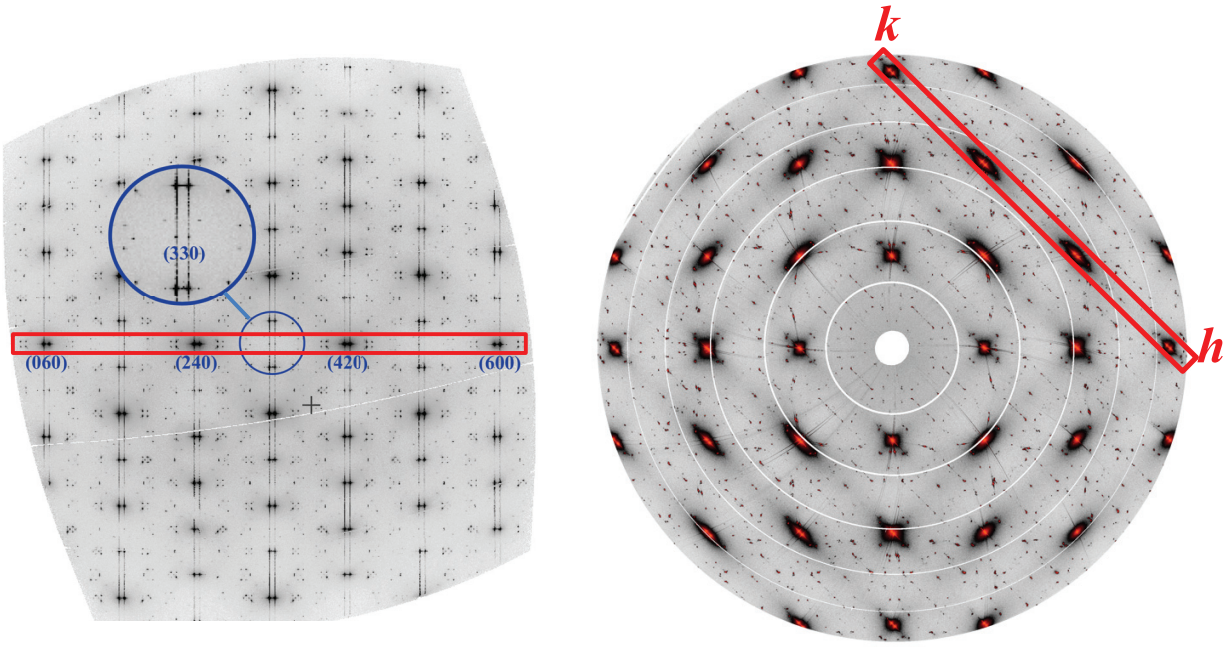

Fig. S3.

Left: Section of the reciprocal lattice from *(600)* to *(060)* in the *(a,b)*-plane, with *[001]* vertical. The plane thus corresponds to a vertical cut of the *(hk0)*-plane as indicated in the right figure by the red box.

Diffuse rods along the c-axis become evident, directly crossing reflections violating *F*-symmetry as for the *(330)*. While the intensity of these "P-type"-reflections is essentially constituted by the diffuse intensity, there is also a significant contribution on the expected P-type reflection position as outlined in the zoomed region (large blue circle) around the *(330)* reflection (small blue circle).

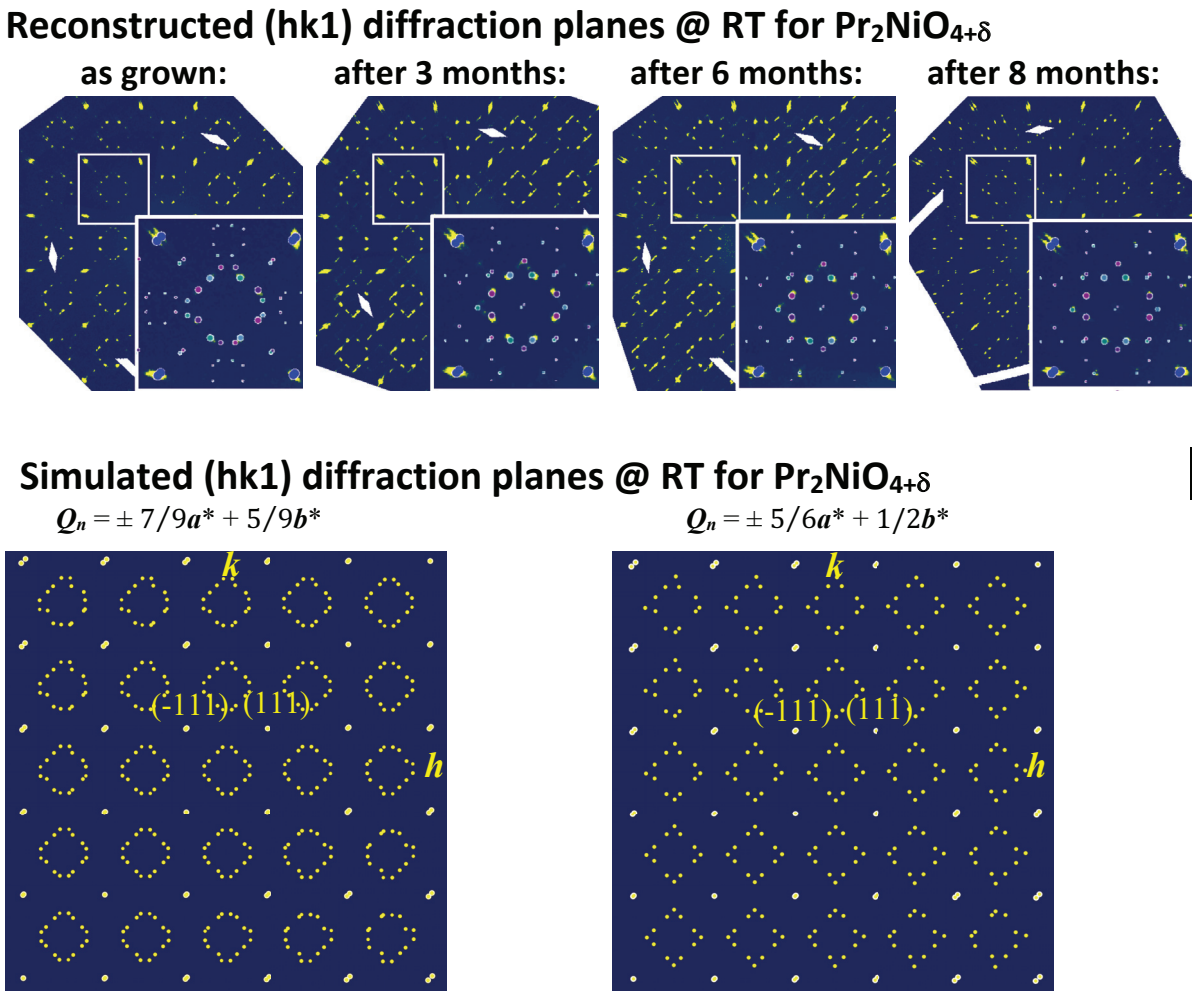

Fig. S4.

Top: *(hk1)*-diffraction planes obtained on a STADIVARI diffractometer, equipped with a Mo μ-focus tube and 2K Pilatus detector for the as grown $Pr_2NiO_{4.25}$ (left) crystal, and after 3, 6, and 8 months, while reaching the final phase corresponding to $Pr_2NiO_{4.225}$. The starting phase $Pr_2NiO_{4.25}$ shows a modulation vector of $\mathbf{Q_n} = \pm 7/9\mathbf{a}^* + 5/9\mathbf{b}^*$ while the end phase $Pr_2NiO_{4.225}$ is characterized by a vector of $\mathbf{Q_n} = \pm 5/6\mathbf{a}^* + 1/2\mathbf{b}^*$. The zoomed square of the as grown crystal is overlaid with the simulated positions of $\mathbf{Q_n} = \pm 7/9\mathbf{a}^* + 5/9\mathbf{b}^*$, while for all other patterns the simulated positions correspond to $\mathbf{Q_n} = \pm 5/6\mathbf{a}^* + 1/2\mathbf{b}^*$. For the figures after 3 and 6 months we can clearly see the progressive evolution of the satellite positions towards the $Pr_2NiO_{4.225}$ final phase following a two phase reaction mechanism. A two-fold orthorhombic twinning with 4 monoclinic twin domains around [010]is taken into account for the simulations. The experimental data are overlayed with the simulated reflection positions while different colours account for different twin domains.

Bottom: Simulated *(hk1)*-planes for the different commensurate modulation vectors of the starting and final-reaction product after oxygen release, taking into account a maximum order for the satellites of m = 2, for simplification. This corresponds to what is essentially obtained from the diffraction data given in top of the figure. Higher order reflections are experimentally observed, but with very weak intensity only. For this reason, they are omitted here in the simulations.

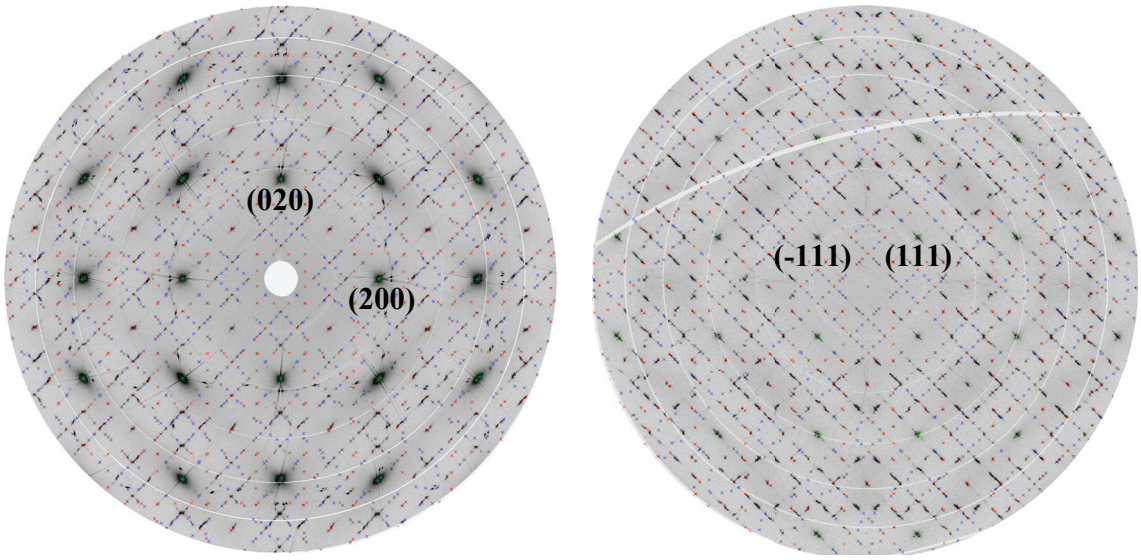

Fig. S5.
Reconstructed *(hk0)* and *(hk1)*-plane of $Pr_2NiO_{4.225}$, obtained on ID29@ESRF at RT. Green crosses correspond to the basic reflections, while red and blue crosses indicate respectively the satellite reflections of the $Pr_2NiO_{4.225}$ (modulation vector $Q_n = \pm 5/6a^* + 1/2b^*$ and a small contamination of $Pr_2NiO_{4.25}$ phase (modulation vector $Q_n = \pm 7/9a^* + 5/9b^*$), both phases simulated up to 5th order). The contamination of the $Q_n = \pm 7/9a^* + 5/9b^*$ satellite reflections for the $Pr_2NiO_{4.225}$ phase is related to a not entirely finalized oxygen release, still containing a minor fraction of the as-grown $Pr_2NiO_{4.25}$ starting crystal.

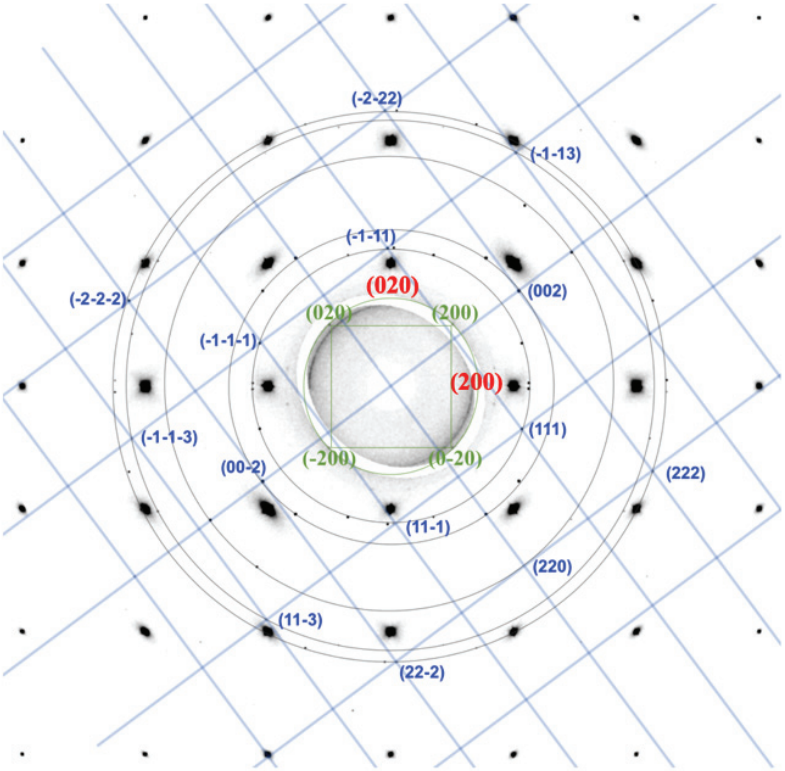

Fig. S6.
Reconstructed *(hk0)*-plane of $Pr_2NiO_{4+\delta}$ obtained from diffraction data on BM01 @ 700°C, (hkl) indexation given in red). This temperature is 800°C and thus 335°C above the monoclinic/tetragonal phase transition at 365°C, so no superstructure reflections related to oxygen ordering are observed any more. The additional reflections are related to a small amount of NiO, which is present as an intergrowth phase following NiO segregation as discussed in [ref. 1]. Totally four domains can be identified, which are twinned around [110], indexation is given in blue for one twin domain out of four. Debye-Scherrer lines of the *(111), (200), (220), (113)* and *(222)* are outlined to better visualize the equivalence by the same scattering angle, all given in blue.
Interestingly there are a few smaller spots with a higher d-value than the (111)-reflection (green), which correspond by their scattering angle and orientation to Ni_3O_4, showing a lattice parameter of 8.20Å, which has so far only been described following irradiation damage of NiO as given in [ref 2-3]. Ni_3O_4 is epitaxially grown on $Pr_2NiO_{4+\delta}$ with $[100]_{Ni3O4}$ parallel to the $[110]_{PNO}$, due to their similar *d*-values: $d_{(200)}Ni_3O_4$ = 4.1 Å, $d_{(220)}$PNO = 3.88Å, resulting into a lattice mismatch of about 5%.

[1] Wahyudi, O. et al. Growth of high quality single crystals of strontium doped (Nd,Pr)-nickelates, $Nd_{2-x}Sr_xNiO_{4+\delta}$ and $Pr_{2-x}Sr_xNiO_{4+\delta}$, Crystengcomm **17**, 6278-6285, doi:10.1039/c5ce00906e (2015)
[2]Buckett, M., & Marks, L. (1988). Formation of a Ni_3O_4 Spinel Phase on the Surface of NiO During Electron Irradiation. MRS Proceedings, 129, 521. doi:10.1557/PROC-129-521
[3] M.I. BUCKETT, et al. Electron Irradiation Damage in Oxides, Ultramicrocopy, 29 (1989), 217-227

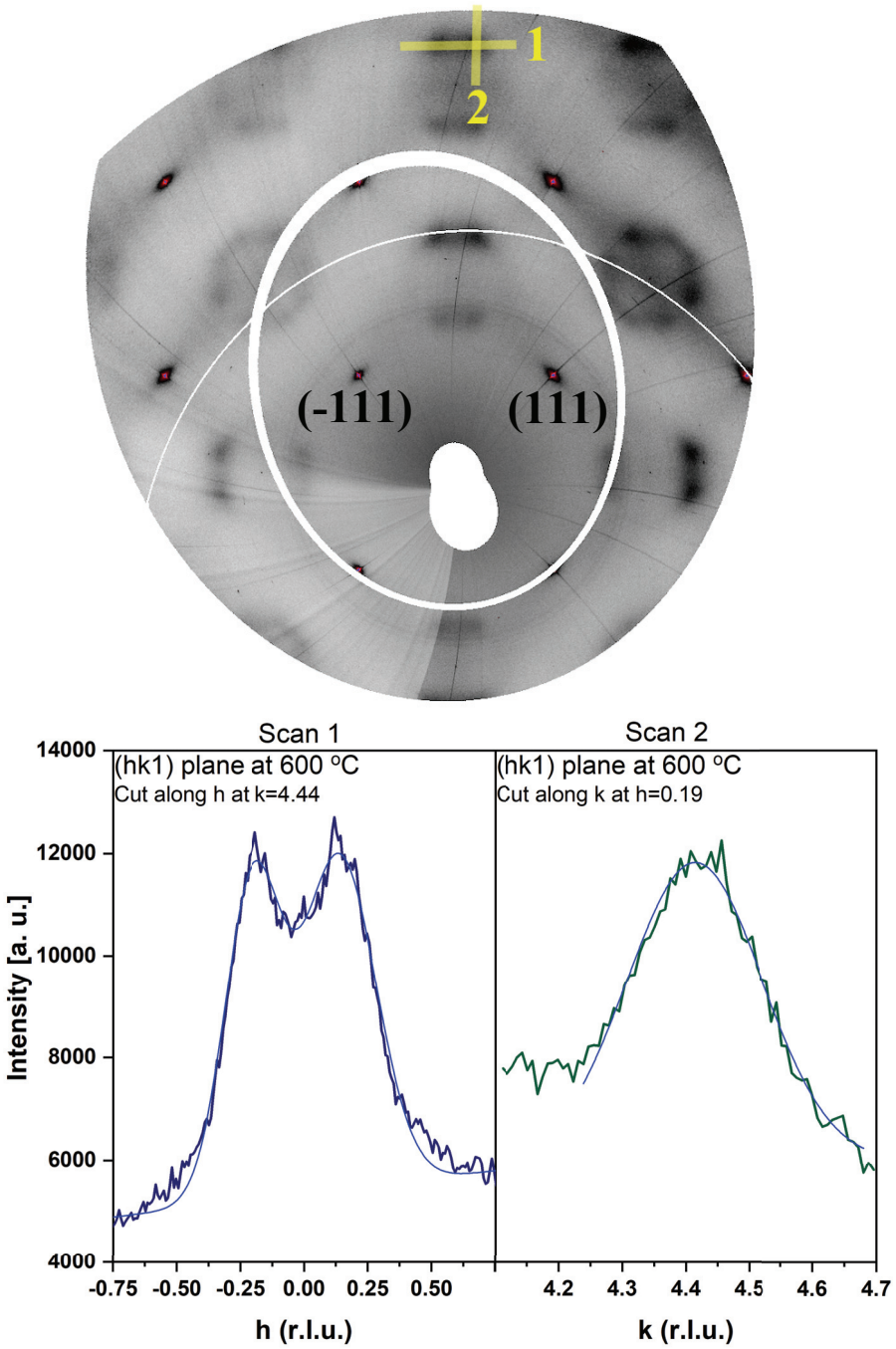

Fig. S7.

Diffuse scattering observed for $Pr_2NiO_{4.25}$ at 600°C. The line profiles indicated for different scan directions are outlined. Correlation lengths become difficult to interpret for double peak structures; we thus considered the "correlation range" as the inverse of the FWHM of the diffuse part under scan 2, which for Gaussian profiles are closely linked by their inversion, yielding 25 Å for the inverse FWHM.

Table S1.
Beamline specifications:

	BM01	**ID23**	**MX - ID29**	**ID28 side station**	**STOE STADIVARI laboratory diffractometer**
Wavelength	0.66305 A	0.688801 A	0.7 A	0.7 A	Microfocus source (Mo) 0.7107 Å
Beam size	~ 70 x 70 μm^2	50µm	50µm	20 x 40 μm^2	~ 150 µm
Detector distance from sample	142 mm	199 mm for RT and 400 mm for LT	250 mm	327 mm	50 mm
Monochromator	Double-crystal Si (111)	Si (111)	Si(111)	C(311)/Si(422)	X-ray fibre optics
Threshold Energy	8997 eV	10800 eV	10627 eV	18000 eV	12000 eV
Exposure time	0.5 s	0.053 s	0.25 s	0.2 s	30 s
Detector	DECTRIS PILATUS 2M (type – pixel, 172 x 172 μm^2)	DECTRIS PILATUS 6M (type – pixel, 172 x 172 μm^2)	DECTRIS PILATUS 6M-F (type – pixel, 172 x 172 μm^2)	DECTRIS PILATUS 1M (type – pixel, 172 x 172 μm^2)	DECTRIS PILATUS 200K (type – pixel, 172 x 172 μm^2)